Nano Research

ISSN 1998-0124 CN 11-5974/O4
https://doi.org/10.26599/NR.2026.94909217

Research Article

# Janus-engineering on the geometrical and electronic characteristics of the lateral and twisted MoSeS/$MoSe_2$ heterostructures investigated by scanning tunneling microscopy

Chenhao Zhang[1,§], Jiangpeng Zhou[1,§], Yanjun Li[1], Zongnan Zhang[1,2](✉), Mengyu Liu[1], Chunmiao Zhang[1], Xuanli Zheng[1], Feiya Xu[1], Lijing Kong[1], Xu Li[1], Zhiming Wu[1], Yaping Wu[1](✉), Junyong Kang[1]

[1] Department of Physics, Engineering Research Centre for Micro-Nano Optoelectronic Materials and Devices at Education Ministry, Fujian Provincial Key Laboratory of Semiconductor Materials and Applications, Xiamen University, Xiamen 361005, China

[2] Beijing National Laboratory for Condensed Matter Physics and Institute of Physics, Chinese Academy of Sciences, Beijing 100190, China

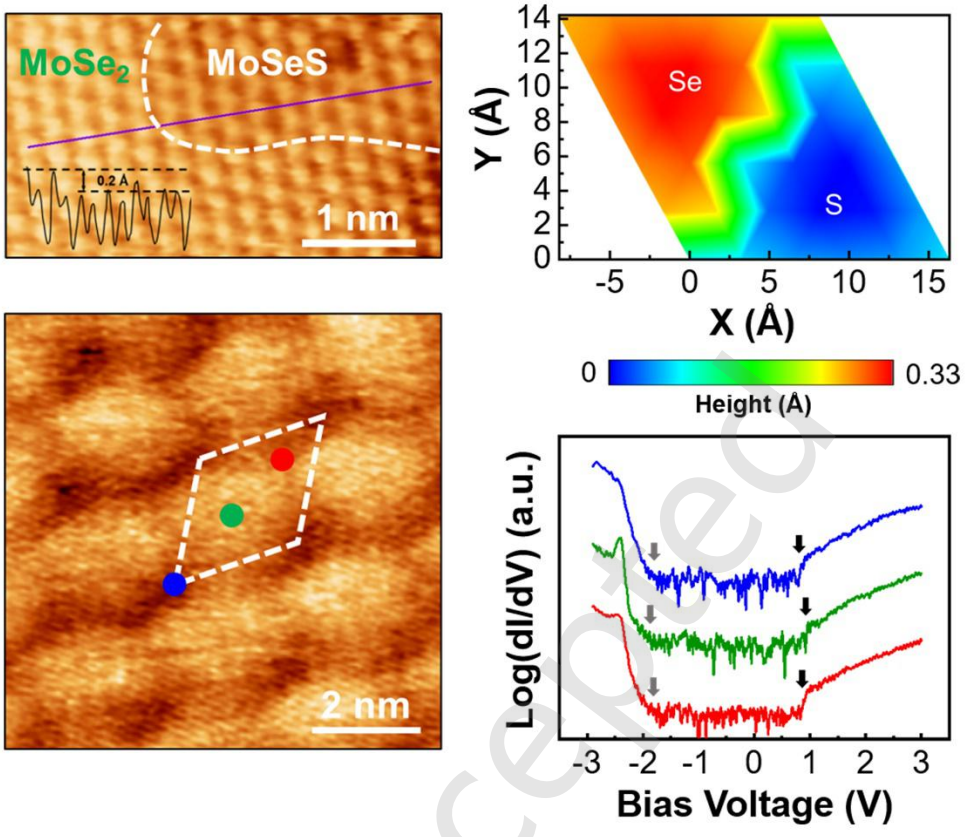
[§] These authors contributed equally to this work.

*Nano Res.*, **Just Accepted Manuscript** • https://doi.org/10.26599/NR.2026.94909217
**https://www.sciopen.com/journal/1998-0124** on Sep. 24, 2026

© The Authors(s)

Just Accepted

This is a "Just Accepted" manuscript, which has been examined by the peer-review process and has been accepted for publication. A "Just Accepted" manuscript is published online shortly after its acceptance,which is prior to technical editing and formatting and author proofing. Tsinghua University Press (TUP) provides "Just Accepted" as an optional and free service which allows authors to make their results available to the research community as soon as possible after acceptance. After a manuscript has been technically edited and formatted, and the page proofs have been corrected, it will be removed from the "Just Accepted" web site and published officially with volume and article number (e.g., *Nano Research*, **2025**, *18*, 94906990). Please note that technical editing may introduce minor changes to the manuscript text and/or graphics which may affect the content, and all legal disclaimers that apply to the journal pertain. In no event shall TUP be held responsible for errors or consequences arising from the use of any information contained in these "Just Accepted" manuscripts. To cite this anuscript please use its Digital Object Identifier (DOI®),which is identical for all formats of publication.




Atomic structures and electronic properties of hydrogen-plasma-synthesized lateral and vertically twisted Janus MoSeS/$MoSe_2$ heterostructures are systematically explored via STM/STS and DFT simulations. Sulfur substitution induces marginal structural discrepancy and bandgap broadening, while moiré stacking and interlayer polarization further modulate the electronic band structure, clarifying the fundamental structure–property relationships of Janus TMDs heterostructures for advanced (opto)electronic and spintronic applications.

Just Accepted

Nano Research

Open Access

Review Article/Research Article Please choose on

# Janus-engineering on the geometrical and electronic characteristics of the lateral and twisted $MoSeS/MoSe_2$ heterostructures investigated by scanning tunneling microscopy

Chenhao Zhang[1,§], Jiangpeng Zhou[1,§], Yanjun Li[1], Zongnan Zhang[1,2] ✉, Mengyu Liu[1], Chunmiao Zhang[1], Xuanli Zheng[1], Feiya Xu[1], Lijing Kong[1], Xu Li[1], Zhiming Wu[1], Yaping Wu[1] ✉ and Junyong Kang[1]

[1] *Department of Physics, Engineering Research Centre for Micro-Nano Optoelectronic Materials and Devices at Education Ministry, Fujian Provincial Key Laboratory of Semiconductor Materials and Applications, Xiamen University, Xiamen 361005, People's Republic of China*
[2] *Beijing National Laboratory for Condensed Matter Physics and Institute of Physics, Chinese Academy of Sciences, Beijing 100190, China*
[§] *These authors contributed equally to this work.*

**Received:** 19 July 2026; **Revised:** 10 September 2026; **Accepted:** 24 September 2026

✉ Address correspondence to Yaping Wu, ypwu@xmu.edu.cn; Zongnan Zhang, zongnan@iphy.ac.cn

**Cite this article:** *Nano Research*, 2026, 19, 94909217 https://doi.org/10.26599/NR.2026.94909217

**ABSTRACT:** Janus transition metal dichalcogenides (TMDs) and their heterostructures offer rich opportunities for property modulation, yet the underlying structural and electronic mechanisms remain elusive. Herein, using scanning tunneling microscopy and spectroscopy (STM/STS), we systematically investigated the structure and electronic state characteristics in lateral and vertically twisted Janus $MoSeS/MoSe_2$ heterostructures fabricated by hydrogen-plasma-assisted sulfurization. Sulfur substitution induces a 0.2 Å reduction in atomic amplitude and a 0.66 eV widening of the bandgap, which density functional theory (DFT) attributes to the electronegativity of substituted atoms and the intrinsic built-in electric field of MoSeS, respectively. In a moiré superlattice of a 7.4°-twisted Janus $MoSeS/MoSe_2$ vertical heterostructure, we identify atomic stacking geometries and stacking- dependent bandgap variations, corroborated by the theoretical simulations. Moreover, the interlayer polarization field arising from stacking further induces nonnegligible modification on the bandgap. This work establishes comprehensive structure-property correlations in Janus $MoSeS/MoSe_2$ heterostructures, providing a solid foundation for the development of advanced Janus TMDs-based electronic and optoelectronic devices.

**KEYWORDS:** $MoSeS/MoSe_2$ heterostructures, scanning tunneling microscopy, built-in electric field, moiré superlattices

## 1 Introduction

Structural symmetry constitutes a fundamental determinant in the electronic, optical, and mechanical properties of two-dimensional (2D) materials[1-5]. Different from conventional transition metal dichalcogenides (TMDs), Janus TMDs possess broken out-of-plane structural symmetry and concomitantly a spontaneous built-in electric field. This unique characteristic originates from the asymmetric sandwich configuration, where transition metal atoms are coordinated by two distinct chalcogen atoms. Since the seminal experimental realization of the Janus MoSeS monolayer via precisely controlled sulfurization of monolayer $MoSe_2$ by Zhang et al.[6], intensive efforts have been devoted to unraveling the novel properties and exploring the applications of Janus TMDs[7-10]. The inherent structural asymmetry endows Janus TMDs with remarkable physical functionalities, including out-of-plane piezoelectric response[11, 12], pronounced Rashba spin splitting[13], and enhanced thermoelectric conversion efficiency[14, 15]. Moreover, a giant room-temperature nonlinear optical response has been observed in non-centrosymmetric 1T' MoSeS, arising from topological band mixing and strong inversion-symmetry breaking induced by the Janus architecture[16]. Additionally, an unconventional $\sqrt{13} \times \sqrt{13}$ charge density wave (CDW) state with broken threefold rotational symmetry has been discovered in monolayer Janus VTeSe[17], which is governed by magnetic-related charge modulation instead of conventional electron-phonon coupling. These exceptional properties establish Janus TMDs as highly promising candidates for next-generation sensors[18], spintronic [19, 20], valleytronic, optoelectronic[21], and catalytic applications[22].

Janus structure engineering has emerged as a versatile strategy for tailoring the electronic structures of heterostructures, thereby enabling the realization of novel functional properties and the optimization of device performance[23-29]. For instance, leveraging the enhanced optical-induced strain sensitivity, the anisotropy and resonance characteristics of second-harmonic generation in 2H- and 3R-stacked Janus $MoSeS/MoS_2$ heterostructures can

Just Accepted

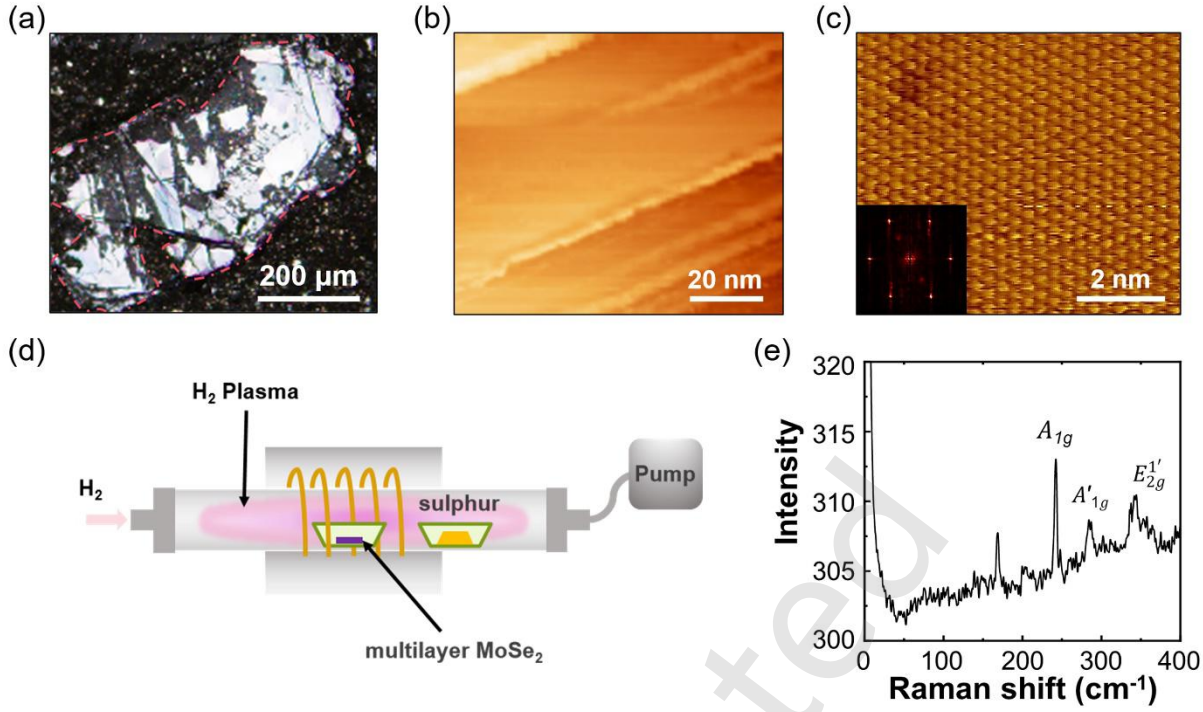



**Fig. 1.** Preparation of the Janus MoSeS on exfoliated $MoSe_2$ crystal. (a) Optical image of the exfoliated multilayer $MoSe_2$. (b) STM image of the exfoliated multilayer $MoSe_2$. (Parameter: $U_b$ = −2.5 V; $I_t$ = −120 pA). (c) Corresponding atom-resolved STM image of the $MoSe_2$ lattice. The inset image is the corresponding FFT image. (Parameter: $U_b$ = −2.0 V; $I_t$ = −85 pA). (d) Schematic diagram of hydrogen-plasma-assisted sulfurization. (e) Raman spectrum of monolayer Janus MoSeS on exfoliated $MoSe_2$ crystal.

be efficiently modulated by varying the incident photon wavelength[30]. Notably, owing to the quantum-confined Stark effect, Janus MoSeS/$MoS_2$ heterostructures exhibit excellent spin-state retention even under the action of strong intrinsic electric fields and thus achieve a maximum intervalley trion valley polarization of 40.2%[31]. In addition, patterned $WS_2$/WSSe lateral heterostructure arrays, produced via a laser-assisted epitaxial regrowth method, allow precise band structures engineering[32]. However, research progress on Janus TMDs systems has so far been confined to theoretical simulations or macroscopic optical characterizations. Probing the electronic properties at the atomic scale is essential not only for uncovering emerging physical phenomena and perfecting the theoretical framework, but also for enhancing the functional performance of electronic and optoelectronic devices. Scanning tunneling microscopy and spectroscopy (STM/STS) offer sub-angstrom spatial resolution, enabling precise mapping of atomic structures and electronic states, which makes them uniquely suited for such investigations. Nevertheless, the fabrication of high- quality Janus materials with atomically flat surfaces remains extremely challenging, and their poor stability poses additional severe obstacles for STM measurements. Consequently, their intrinsic electronic structures, especially twist-modulated interfacial behaviors in moiré superlattices, remain largely unexplored. This knowledge gap severely hampers our in-depth understanding of interfacial modulation and impedes the rational design and performance optimization of Janus-based functional devices.

In this work, we systematically address these critical issues by comprehensively investigating the structural and electronic characteristics of both lateral and vertically twisted Janus MoSeS/$MoSe_2$ heterostructures via STM and STS. Our experimental observations unambiguously reveal a 0.2 Å reduction in atomic amplitude and a 0.66 eV widening of the bandgap in lateral Janus heterostructures. Such variations originate primarily from the electronegativity of substituted sulfur atoms and the intrinsic built-in electric field of MoSeS based on the density functional theory (DFT) analyses. More importantly, we unambiguously identify the atomic stacking configurations and stacking-dependent bandgap modulation in a 7.4°-twisted vertical Janus MoSeS/$MoSe_2$ heterostructure, with excellent agreement between STM results and theoretical simulations. Our work not only elucidates the intrinsic electronic behaviors of Janus TMDs heterostructures but also provides a robust guideline for the rational design of high-performance functional devices based on this emerging material platform.

## 2 Results and discussion

Janus MoSeS/$MoSe_2$ heterostructures were constructed from mechanically exfoliated $MoSe_2$ crystals. For conducting STM measurements, few-layer and thicker $MoSe_2$ flakes were obtained using an improved exfoliation approach that employs an adhesion layer as a mediator (details in Fig. S1 in the Supplementary Material). As shown in Fig. 1(a), the exfoliated $MoSe_2$ flake exhibits an irregular shape with an area of approximately 15.4 $mm^2$. The weakly transparent contrast in the optical image corresponds to few-layer $MoSe_2$, while the blue or white regions indicate thicker areas. Figure 1(b) presents the corresponding STM image of this exfoliated $MoSe_2$ crystal, revealing a flat and uniform surface morphology with sharp steps. The atomic lattice constant is

Just Accepted

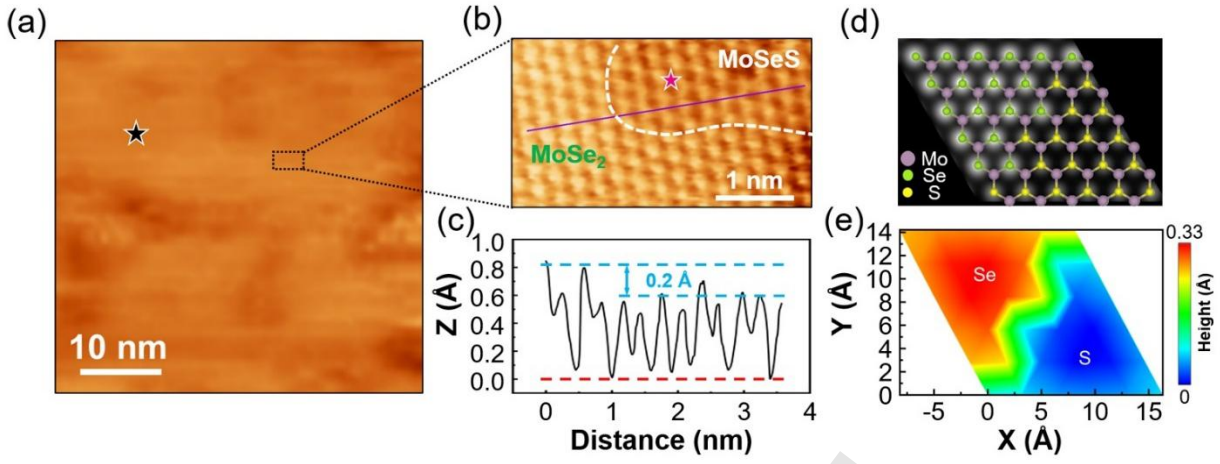



**Fig. 2.** Surface morphologies after sulfurization. (a) STM image of multilayer $MoSe_2$ after sulfurization. (Parameter: $U_b$ = 2.0 V; $I_t$ = 33 pA). (b) Atom-resolved STM image of MoSeS/$MoSe_2$ lateral heterostructure. (Parameter: $U_b$ = 2.5 V; $I_t$ = 100 pA). (c) Height profile along the purple line in (b). (d) Simulated STM image of MoSeS/$MoSe_2$ lateral heterostructure. (e) Simulated height variation of the surface atoms in the lateral heterostructure.

determined to be 3.01 Å from the atom- resolved STM image in Fig. 1(c) and its corresponding fast Fourier transform (FFT) pattern.

To synthesize Janus MoSeS monolayers, a hydrogen-plasma-assisted sulfurization strategy was employed to selectively replace the top-layer Se atoms of pristine $MoSe_2$[33], as depicted in Fig. 1(d). Specifically, the exfoliated multilayer $MoSe_2$ flakes were placed upstream in the plasma-assisted chemical vapor deposition system, while sulfur powder was loaded downstream. After the chamber was evacuated to its base pressure, $H_2$ plasma was generated by dissociating 20 sccm $H_2$ under a radiofrequency (RF) power. The sulfurization reaction was conducted at room temperature. During the reaction, hydrogen selenide species formed and desorbed from the $MoSe_2$ surface, creating selenium vacancies that were subsequently filled by sulfur atoms, thereby achieving elemental substitution on the $MoSe_2$ surface.

By tuning the RF power and sulfurization duration, we achieved the controlled synthesis of Janus MoSeS with tunable elemental ratios. The sulfur substitution level could be quantified by fitting the characteristic peaks of Mo, S, and Se, as shown in Fig. S2. Accordingly, a 15% coverage of Janus MoSeS was obtained by optimizing the sulfurization parameters, which enables the construction of MoSeS/$MoSe_2$ lateral Janus heterostructures on the surface of exfoliated $MoSe_2$ multilayer (Fig. 1(a)). As confirmed by Raman spectroscopy (Fig. 1(e)), in addition to the characteristic out-of-plane mode ( $A_{1g}$) of multilayer $MoSe_2$ at 242.3 $cm^{-1}$, new peaks emerged after sulfurization. A peak at 287.0 $cm^{-1}$ was assigned to the out-of-plane mode ($A'_{1g}$) of Janus MoSeS, and another at 354.8 $cm^{-1}$ corresponding to the in-plane mode ( $E^{1'}_{2g}$ ), in agreement with previous reports[34].

Upon hydrogen-plasma-assisted sulfurization, the surface morphology underwent significant modification. As displayed in Fig. 2(a), numerous defects and cracks, along with local clusters, are randomly distributed on the treated surface, originating from both plasma irradiation and the incomplete S-atom substitution process. To gain deeper insight into the atomic structural evolution induced by sulfurization, atom-resolved STM imaging was performed on a flat and clean surface region. Remarkably, a subtle contrast variation was clearly resolved across the interface between MoSeS and $MoSe_2$ (highlighted by the white dotted line in Fig. 2(b)). The height profile extracted along the purple line in Fig. 2(b) reveals a marginal height difference of approximately 0.2 Å across the boundary of the MoSeS/$MoSe_2$ lateral heterostructure (see Fig. 2(c)). To verify the experimental observations, a 5×5 MoSeS/$MoSe_2$ lateral heterostructure model was constructed, and the corresponding STM image was simulated, as presented in Fig. 2(d). The simulated STM image exhibits distinct contrast, where the $MoSe_2$ domain is slightly brighter than the adjacent MoSeS region. The quantitative height difference of the simulated heterostructure was further evaluated in Fig. 2(e), yielding a maximum height difference of approximately 0.3 Å between $MoSe_2$ and MoSeS domains, in good agreement with the experimental measurements. The observed contrast difference in the MoSeS/$MoSe_2$ lateral heterostructure is fundamentally attributed to the higher electronegativity of S atoms, which gives rise to a smaller atomic radius and a shorter Mo-S bond length (2.41 Å) compared with the Mo-Se bond (2.54 Å). This interpretation is further supported by previous studies on Se substitution on Te film surface[35].

We next systematically probed the electronic structures of the $MoSe_2$ and MoSeS regions using STS. For the multilayer $MoSe_2$ shown in Fig. 2(a), the dI/dV spectrum exhibits a bandgap of 1.25 eV (Fig. 3(a)), with the conduction band minimum (CBM) at 0.68 eV and the valence band maximum (VBM) at −0.57 eV, indicative of a weak p-type doping characteristic in the exfoliated multilayer $MoSe_2$. In contrast, the dI/dV spectrum acquired from the MoSeS region reveals a substantially wider bandgap of 1.85 eV, with the CBM and VBM located at 0.62 eV and −1.23 eV, respectively (Fig. 3(b)). For simplicity, we employed AB- stacked bilayer (BL) $MoSe_2$ and the MoSeS/$MoSe_2$ heterostructure for band- structure simulations via the Heyd-Scuseria-Ernzerhof (HSE06) method (Fig. 3(c), (d)), aiming to elucidate the origin of the prominent bandgap expansion observed in the MoSeS region. In this stacking configuration, the Se atoms of the top layer are vertically aligned with the Mo atoms of the underlying layer. As displayed, BL-$MoSe_2$ shows an indirect bandgap of 2.11 eV, whose CBM lies between K and Gamma (G) points

Just Accepted

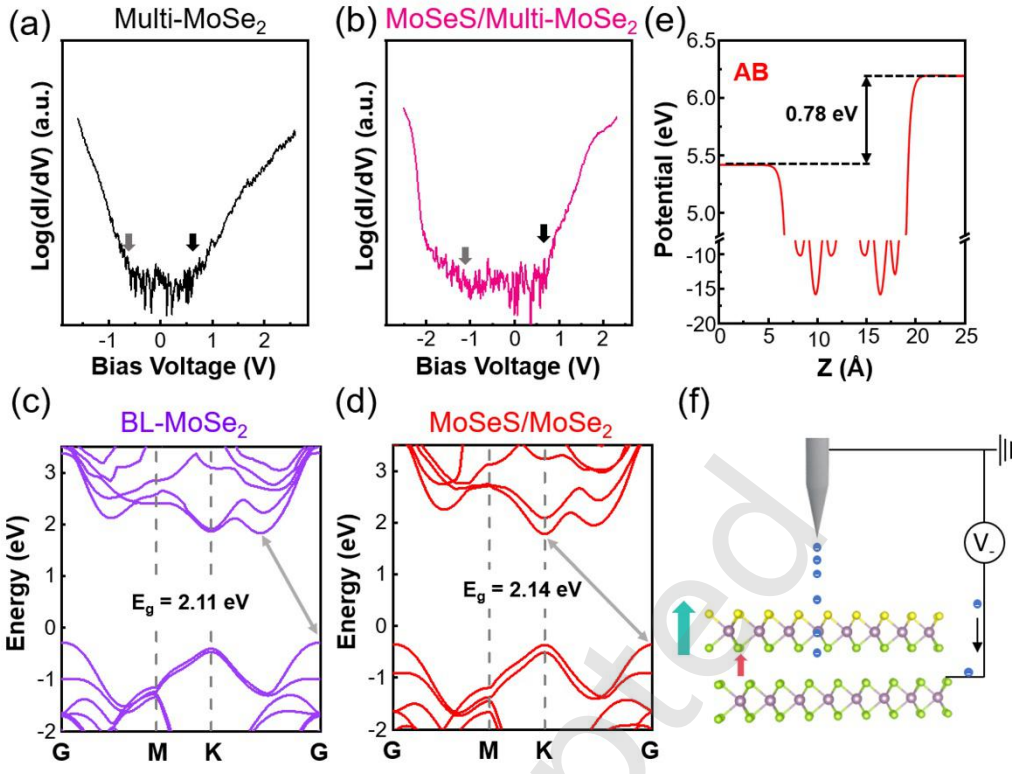



**Fig. 3.** Electronic characteristics of the Janus MoSeS. (a, b) dI/dV spectra of multilayer $MoSe_2$ and MoSeS/multilayer $MoSe_2$, collected at the positions marked in Fig. 2(a) and (b), respectively (Parameter: $U_b$ = 2.2 V; $I_t$ = 230 pA). (c, d) Calculated band structures of bilayer $MoSe_2$ and MoSeS/$MoSe_2$ heterostructure with the AB stacking. (e) Planar-averaged electrostatic potential along the out-of-plane (Z) direction of the AB-stacked MoSeS/$MoSe_2$ heterostructure. (f) Schematic diagram of the electron tunneling process under a negative bias; the green and red arrows mark the direction of intrinsic built-in electric field of MoSeS and interlayer polarized field; the black arrow indicates the direction of electron transport.

and VBM positions at G point. As for MoSeS/$MoSe_2$ heterostructure, the indirect bandgap remains except for a shift of the CBM to the K point and a slightly widened bandgap of 2.14 eV. To rationalize the considerable bandgap difference arising from the formation of Janus MoSeS, we further explored the effect of lattice strain on the band structure by taking account of the lattice mismatch within the MoSeS/$MoSe_2$ heterostructure. As shown in Fig. S3, lattice strain alters the band structure of the heterostructure but yields only limited bandgap variations. These theoretical results reveal that BL-$MoSe_2$ and the MoSeS/$MoSe_2$ heterostructure possess comparable bandgaps, demonstrating that the experimentally observed bandgap discrepancy does not originate from their intrinsic electronic band structures.

We therefore turned to structural differences to identify the underlying mechanism. Unlike the symmetric $MoSe_2$, Janus MoSeS hosts a spontaneous built-in electric field originating from the electronegativity mismatch between S and Se atoms. This intrinsic electric field points from Se to S atoms, giving rise to a substantial potential drop across the S-Se atomic plane. For the AB-stacked MoSeS/$MoSe_2$ heterostructure, the calculated interfacial potential difference reaches 0.78 eV (Fig. 3(e)). Given that interlayer stacking can modulate the interfacial potential, another heterostructure with AC stacking, where the Se atom in the upper layer is aligned with the Mo atom in the underneath layer, was also calculated for comparison (Fig. S4), yielding a potential height of 0.69 eV. The intrinsic potential height of Janus MoSeS is estimated to be 0.74 eV, consistent with the result in Fig. S4(c). Therefore, the observed bandgap enlargement in the MoSeS region can be mainly attributed to the additional interfacial potential induced by S-atom substitution. This physical picture is schematically illustrated in Fig. 3(f). Under a negative bias, tunneling electrons require an extra voltage to overcome the intrinsic built-in electric field within the MoSeS layer before reaching the STM tip; whereas under a positive bias, electrons tunneling from the tip to the sample can readily traverse the MoSeS layer. Accordingly, the experimental interfacial potential of the MoSeS layer is derived to be 0.66 eV by comparing the VBM positions of $MoSe_2$ and MoSeS regions, in good agreement with the theoretical prediction.

To explore the moiré characteristics in the Janus MoSeS/$MoSe_2$ heterostructure, we intentionally introduced interlayer shear strain to construct a controllable interlayer twist angle[36, 37]. This twist angle can be tuned by adjusting the peeling direction of adhesive tape during mechanical exfoliation. By further optimizing the hydrogen-plasma-assisted sulfurization process, a twisted Janus MoSeS/$MoSe_2$ vertical heterostructure with improved substitution ratio and crystal quality was successfully obtained. Figure 4(a) presents a moiré superlattice of Janus MoSeS/$MoSe_2$ heterostructure with a periodicity of 2.27 nm. The twist angle is calculated to be 7.4° using the formula:

$$\lambda = \frac{(1+\delta)a}{\sqrt{2(1+\delta)(1-cos\theta)+\delta^2}} \qquad (1)$$

here $\lambda$ is the moiré period, $a$ is the lattice constant of $MoSe_2$, $\delta$ denotes the lattice mismatch between $MoSe_2$ and MoSeS, and $\theta$ represents the interlayer twist angle. The corresponding atomic

Just Accepted

model was then constructed, as shown in Fig. 4(b). Beyond the AB and AC stackings, there exists another typical

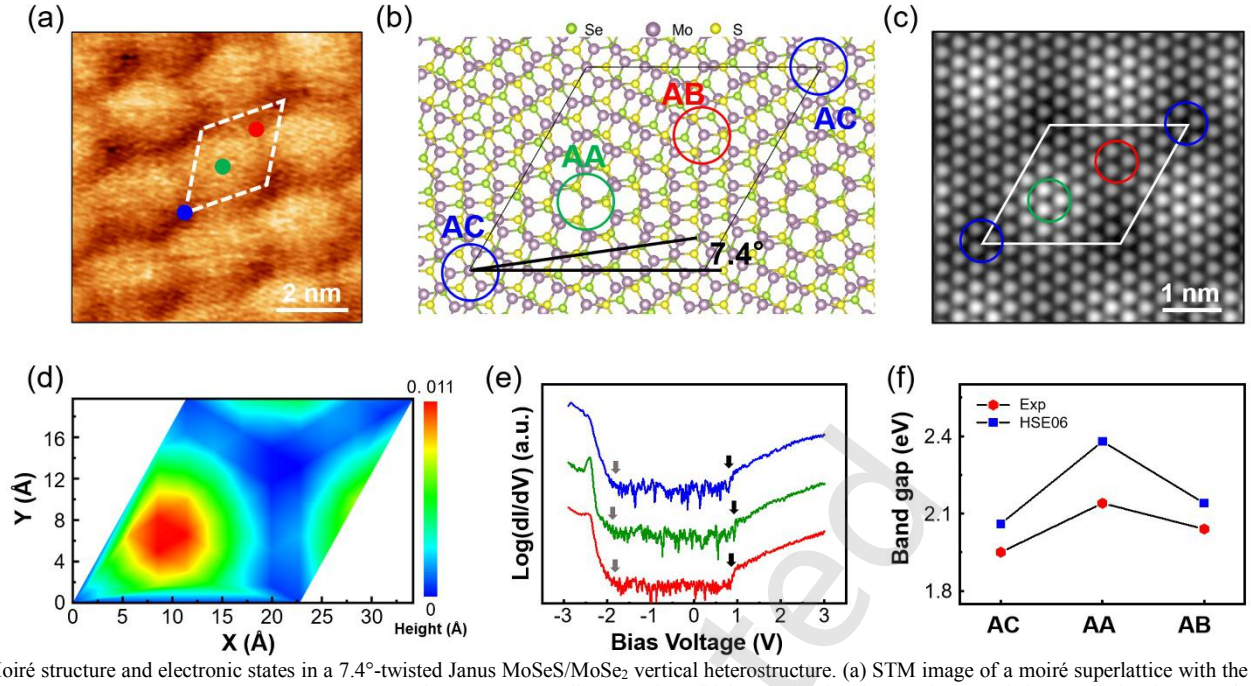



**Fig. 4.** Moiré structure and electronic states in a 7.4°-twisted Janus MoSeS/$MoSe_2$ vertical heterostructure. (a) STM image of a moiré superlattice with the twist angle of 7.4°. (Parameter: $U_b$ = 2.2 V; $I_t$ = 155 pA). (b, c) Corresponding atomic model and simulated STM image of the 7.4°-twisted MoSeS/$MoSe_2$ heterostructure. (d) Height variation of the surface atoms in a simulated twisted heterostructure. (e) dI/dV spectra acquired at three characteristic positions of the moiré superlattice in (a) (Parameter: $U_b$ = 2.2 V; $I_t$ = 230 pA). (f) Comparison of the experimental and theoretical bandgaps.

stacking with the Se atoms of the upper and lower layers vertically aligned, named AA stacking. Theoretical simulations of STM images were further performed for this twisted heterostructure. As shown in Fig. 4(c), the simulated STM image displays a well-defined moiré superlattice, in which the AA stacking region exhibits a distinctly brighter contrast than the other regions. Figure 4(d) depicts the height variation distribution of surface S atoms in the simulated moiré superlattice. Notably, a maximum height difference occurs at the AA site, due to the stronger repulsive interaction between interfacial Se atoms of the two layers. By combining experimental observations with theoretical simulations, the precise atomic registry of the observed superlattice is unambiguously determined.

We further systematically explored the site-dependent electronic properties of the AA, AB, and AC stacking configurations by combining STS characterization with theoretical calculations. As displayed in Fig. 4(e), the three stacking configurations exhibit nearly identical electronic state distributions above the CBM while distinct discrepancies below the VBM. In particular, the electronic state around −2.41 eV shows a clear site-related intensity evolution, which exhibits a sharp peak for AA stacking, a weakened peak for AB stacking, and complete suppression for AC stacking. Based on the simulated spatial height variation in Fig. 4(d), such site-modulated electronic state behavior is primarily attributable to moiré-induced lattice strain. Meanwhile, slight shifts in the CBM and VBM positions were also observed among the three stackings, resulting in distinct bandgap values. The AA stacking possesses the widest bandgap of 2.80 eV, whereas the AB and AC stackings show comparable bandgaps of 2.70 eV and 2.61 eV, respectively. As mentioned above, the intrinsic built-in electric field in MoSeS layer introduces an additional voltage offset that effectively enlarges the measured bandgap. After eliminating the contribution of the built-in electric field, the intrinsic bandgaps of AA, AB, and AC stackings are calibrated to 2.14 eV, 2.04 eV, and 1.95 eV, respectively. To further elucidate the site-dependent electronic states in this moiré superlattice, we additionally calculated the band structures of the AA and AC stackings (Fig. S5). As shown, the band structures are strongly dependent on stacking configurations. The AA- stacked MoSeS/$MoSe_2$ heterostructure exhibits a direct bandgap of 2.38 eV, whereas the AC- stacked counterpart features an indirect bandgap of 2.06 eV. These values show good consistency with experimental observations, further verifying the site- dependent bandgap modulation in twisted MoSeS/$MoSe_2$ hetero structures. The experimental and calculated bandgap results are summarized in Fig. 4(f). Additionally, the distinct bandgap behaviors of AB and AC stackings can be rationalized in terms of their opposite interlayer polarization field and differing interlayer coupling, as the calculated potential height of AA stacking is comparable to that in the Janus MoSeS monolayer (see Fig. 3(e) and Fig. S4).

## 3 Conclusions

In summary, Janus MoSeS was successfully fabricated on exfoliated multilayer $MoSe_2$ via hydrogen-plasma-assisted sulfurization. Upon S-atom substitution, prominent structural and electronic modifications were clearly resolved by STM and STS measurements, manifested as a 0.2 Å reduction in atomic amplitude and a 0.66 eV widening of the bandgap. DFT calculations confirm that the intrinsic built-in electric field within MoSeS layer introduces an additional voltage offset, which accounts for the observed bandgap enlargement. Moreover, the moiré features of the vertically stacked Janus MoSeS/$MoSe_2$ heterostructure with a twist angle of 7.4° were systematically elucidated. Combined with theoretical

Just Accepted

simulations, the atomic registry of the observed moiré superlattice was unambiguously identified, and stacking-dependent bandgap modulation was unequivocally demonstrated. Additionally, the stacking-induced interlayer polarization field, along with interlayer coupling, further contributes to the observed bandgap modulation. This work provides a comprehensive understanding of the structural and electronic properties of both lateral and vertical Janus MoSeS/$MoSe_2$ heterostructures, and establishes a robust framework for the design of advanced optoelectronic and electronic devices based on Janus TMDs platforms.

## 4 Experiments and calculations

### 4.1 Computational Details

The electronic structures of the investigated systems were examined within the framework of DFT as implemented in the Vienna ab initio Simulation Package (VASP)[38]. The interaction between ions and electrons was described via the projector augmented-wave (PAW) method[39], while the exchange-correlation energy was treated within the generalized gradient approximation (GGA) of Perdew-Burke-Ernzerhof (PBE)[40]. A vacuum layer of 20 Å was introduced along the out-of-plane direction to eliminate spurious interactions between periodically repeated cells. The plane-wave kinetic energy cutoff was set to 500 eV, and the electronic energy convergence criterion was set to $10^{-6}$ eV per unit cell. Structural optimizations were performed until the residual force on each atom was less than 0.01 eV/Å. A 1×1 bilayer $MoSe_2$ primitive cell and a vertically stacked MoSeS/$MoSe_2$ heterostructure were constructed, and their Brillouin zones were sampled using a Γ-centered 13×13×1 Monkhorst-Pack k-point mesh. For the MoSeS/$MoSe_2$ moiré superlattice with a twist angle of 7.4°, a Γ-centered 1×1×1 Monkhorst-Pack k-point mesh was employed considering the large lattice periodicity and the increased number of atoms in the supercell. To simulate partially sulfur-substituted MoSeS heterostructures, a 6×6×1 lateral MoSeS/$MoSe_2$ heterostructure was constructed and sampled using a Γ-centered 3×3×1 Monkhorst-Pack k-point mesh. The DFT-D3 method was considered to correct the van der Waals interactions[41]. The simulated STM images were performed using the Tersoff-Hamann framework[42]. The HSE06 hybrid functional[43] was adopted to obtain the accurate band structures of AA-, AB-, and AC-stacked MoSeS/$MoSe_2$ heterostructures, so as to elucidate the site- dependent bandgap modulations.

### 4.2 STM Measurements

The as-prepared sample was transferred into a scanning tunneling microscope (STM, Unisoku, USM1300) for characterization. STM measurements were performed in the constant-current mode at a cryogenic temperature of approximately 78 K under an ultrahigh vacuum (UHV) environment with a base pressure of $6\times10^{-11}$ torr. A bias voltage was applied to the sample relative to the grounded STM tip. To facilitate measurement, the exfoliated multilayer flakes were loaded at the center of the scanning window of the sample holder before transferring into the STM scan head. Prior to electronic structure characterizations, electrochemically etched tungsten (W) tips were employed and calibrated on a clean Au (111) crystal surface. The dI/dV spectra were acquired via a lock-in amplifier technique in the constant-height mode, with a peak-to-peak modulation amplitude of 20 mV and a modulation frequency of 957 Hz.

**Electronic Supplementary Material**: Supplementary material (schematic illustration and procedural details of the improved mechanical exfoliation method for STM characterization, XPS characterization and peak fitting for elemental substitution in monolayer MoSeS, effect of lattice mismatch on the band structures of MoSeS/$MoSe_2$ heterostructure, calculated band structures of AA- and AC-stacked $MoSe_2$/MoSeS heterostructures, and planar-averaged electrostatic potentials of AA- and AC-stacked $MoSe_2$/MoSeS heterostructures and monolayer MoSeS) is available in the online version of this article at https://doi.org/10.26599/NR.2026.94909217.

## Data availability

All data needed to support the conclusions in the paper are presented in the manuscript and/or the Electronic Supplementary Material. Additional data related to this paper may be requested from the corresponding author upon request.

## Acknowledgements

The work is supported by the National Natural Science Foundation of China (grant nos. 62574174, 62274139, 62304188, 62374144, and 62374143), the Natural Science Foundation of Fujian Province (No. 2025J011001), the Natural Science Foundation of Xiamen (No. 3502Z20227009), and the Basic Research Funds for Central Universities (Grant No. 20720220025).

## Declaration of competing interest

All the contributing authors report no conflict of interests in this work.

## Author contribution statement

Chenhao Zhang: Conceptualization, Investigation, Formal analysis. Jiangpeng Zhou: Formal analysis, Visualization, Writing - original draft. Yanjun Li: Methodology, Formal analysis. Zongnan Zhang: Supervision, Data curation, Formal analysis, Writing - original draft, Writing - review & editing. Mengyu Liu: Conceptualization, Methodology. Chunmiao Zhang: Resources. Xuanli Zheng: Methodology. Feiya Xu: Resources. Lijing Kong: Resources. Xu Li: Supervision, Conceptualization. Zhiming Wu: Supervision, Conceptualization. Yaping Wu: Supervision, Conceptualization, Funding acquisition, Formal analysis, Writing - review & editing. Junyong Kang: Supervision, Conceptualization. The manuscript was written through contributions from all authors. All authors have approved the final manuscript.

## Use of AI statement

None.

## References

[1] Fu, J. H.; Kuisma, M.; Larsen, A. H.; Shinohara, K.; Togo, A.; Thygesen, K. S. Symmetry classification of 2d materials: Layer groups versus space groups. *2D Materials* **2024**, 11, 035009.
[2] Lleopart, G.; Alcón, I.; Moreira, I. D. R.; Bromley, S. T. Using sublattice symmetry breaking to tune the electronic structure and chemical stability of si-substituted carbon-based 2d materials. *2D Materials* **2026**, 13, 025030.
[3] Sun, Z. L.; Ye, G. H.; Wan, X. H.; Mao, N.; Nnokwe, C.; Li, S. L.; Agarwal, N.; Sarkar, S.; Zhai, Z. X.; Lv, B. et al. Tunable symmetry breaking in a hexagonal-stacked moiré magnet. *Nature Physics* **2026**, 22, 870-876.

Just Accepted

[4] Xu, S. H.; Chu, S. B.; Mrad, R.; Zhang, Z. J.; Li, Z. L.; Jiao, R. X.; Chen, Y. P. Discovery of 2d materials via symmetry-constrained diffusion model. *Journal of Physical Chemistry C* **2025**, 129, 6794-6802.
[5] Zhang, Y. J.; Kamiya, K.; Yamamoto, T.; Sakano, M.; Yang, X. H.; Masubuchi, S.; Okazaki, S.; Shinokita, K.; Chen, T. M.; Aso, K. et al. Symmetry engineering in twisted bilayer $wte_2$. *Nano Letters* **2023**, 23, 9280-9286.
[6] Zhang, J.; Jia, S.; Kholmanov, I.; Dong, L.; Er, D.; Chen, W.; Guo, H.; Jin, Z.; Shenoy, V. B.; Shi, L. et al. Janus monolayer transition-metal dichalcogenides. *ACS Nano* **2017**, 11, 8192-8198.
[7] Ahmad, W.; Wang, Y.; Kazmi, J.; Younis, U.; Mubarak, N. M.; Aleithan, S. H.; Channa, A. I.; Lei, W.; Wang, Z. M. Janus 2d transition metal dichalcogenides: Research progress, optical mechanism and future prospects for optoelectronic devices. *Laser & Photonics Reviews* **2025**, 19, 2400341.
[8] Shi, W. W.; Li, G. Q.; Wang, Z. G. Triggering catalytic active sites for hydrogen evolution reaction by intrinsic defects in janus monolayer mosse. *Journal of Physical Chemistry C* **2019**, 123, 12261-12267.
[9] Xia, C. X.; Xiong, W. Q.; Du, J.; Wang, T. X.; Peng, Y. T.; Li, J. B. Universality of electronic characteristics and photocatalyst applications in the two-dimensional janus transition metal dichalcogenides. *Physical Review B* **2018**, 98, 165424.
[10] Zhao, G. D.; Fu, W. D.; Li, Y. C.; Liu, X. E.; Jia, F. H.; Hu, T.; Ren, W. Hidden valley polarization, piezoelectricity, and dzyaloshinskii-moriya interactions of janus vanadium dichalcogenides. *ACS Applied Materials & Interfaces* **2023**, 16, 1268-1275.
[11] Dong, L.; Lou, J.; Shenoy, V. B. Large in-plane and vertical piezoelectricity in janus transition metal dichalchogenides. *ACS Nano* **2017**, 11, 8242-8248.
[12] Ma, B.; Cui, S. X.; Zhao, B.; Zhang, G. Q.; Guo, F.; Li, J.; Wang, X. C. Coexistence of in-plane and out-of-plane piezoelectricity in janus $wxsin_2$ (x = s, se, te) monolayers: Potential implications for nanoscale piezoelectric devices. *ACS Applied Nano Materials* **2025**, 8, 4876-4884.
[13] Cheng, Y. C.; Zhu, Z. Y.; Tahir, M.; Schwingenschlögl, U. Spin-orbit-induced spin splittings in polar transition metal dichalcogenide monolayers. *EPL* **2013**, 102, 57001.
[14] Lu, S.; Ren, W. J.; He, J.; Yu, C. Q.; Jiang, P. F.; Chen, J. Enhancement of the lattice thermal conductivity of two-dimensional functionalized mxenes by inversion symmetry breaking. *Physical Review B* **2022**, 105, 165301.
[15] Xia, Q.; Liu, Y. S.; Gao, G. Y. Enhanced thermoelectric performance and reversed anisotropy in the janus penta-pdsete monolayer via biaxial strain. *Journal of Materials Chemistry C* **2025**, 13, 5689-5699.
[16] Shi, J.; Xu, H.; Heide, C.; HuangFu, C.; Xia, C.; de Quesada, F.; Shen, H.; Zhang, T.; Yu, L.; Johnson, A. et al. Giant room-temperature nonlinearities in a monolayer janus topological semiconductor. *Nature Communications* **2023**, 14, 4953.
[17] Xu, Z. Q.; Shao, Y.; Huang, C.; Zhu, C.; Hu, G. Y.; Hu, S. H.; Li, Z. L.; Hao, X. Y.; Hou, Y. H.; Zhang, T. et al. Unusual charge density wave introduced by the janus structure in monolayer vanadium dichalcogenides. *Science Advances* **2025**, 11, eadq4406.
[18] Chaurasiya, R.; Dixit, A. Defect engineered mosse janus monolayer as a promising two dimensional material for $no_2$ and no gas sensing. *Applied Surface Science* **2019**, 490, 204-219.
[19] Chen, E. Z.; Zhu, Q.; Duan, Y. Y.; Tang, J. H.; Zhan, R. Z.; Huang, J. W.; Wan, X.; Chen, K.; Deng, S. Z. Janus electronic devices with ultrathin high-κ gate dielectric directly integrated on 1t′-$mote_2$. *ACS Applied Materials & Interfaces* **2024**, 16, 68211-68220.
[20] Vojácek, L.; Dueñas, J. M.; Li, J.; Ibrahim, F.; Manchon, A.; Roche, S.; Chshiev, M.; García, J. H. Field-free spin-orbit torque switching in janus chromium dichalcogenides. *Nano Letters* **2024**, 24, 11889-11894.
[21] Liu, C.; Liang, T.; Sui, X.; Du, L.; Guo, Q.; Xue, G.; Huang, C.; You, Y.; Yao, G.; Zhao, M. et al. Anomalous photovoltaics in janus mosse monolayers. *Nature Communications* **2025**, 16, 544.
[22] Kim, S. W.; Choi, S. Y.; Lim, S. H.; Ko, E. B.; Kim, S.; Park, Y. C.; Lee, S.; Kim, H. H. Understanding solvent-induced delamination and intense water adsorption in janus transition metal dichalcogenides for enhanced device performance. *Advanced Functional Materials* **2024**, 34, 2308709.
[23] Kopaczek, J.; Sayyad, M. Y.; Sailus, R.; Wu, C. L.; Moosavy, S. T. R.; Ruddick, H.; Kudrawiec, R.; Tongay, S. A. Promoting interlayer exciton in janus/transition metal dichalcogenide heterostructures by annealing. *ACS Applied Electronic Materials* **2025**, 7, 997-1003.
[24] Li, Y. N.; Yan, Z. H.; Wang, S. D. Spin character of interlayer excitons in tungsten dichalcogenide heterostructures: Gw-bse calculations. *Physical Review B* **2024**, 109, 045422.
[25] Sgouros, A. P.; Michos, F. I.; Sigalas, M. M.; Kalosakas, G. Thermal relaxation in janus transition metal dichalcogenide bilayers. *Materials* **2024**, 17, 4200.
[26] Wang, Y. L.; Liu, H. G.; Ji, H. H.; Bo, Y. F.; Zhang, Y. J.; Yang, X. D.; Shen, Y. Tunable optoelectronic properties of janus wsete/g-gan van der waals heterostructures by strain engineering. *Materials Today Communications* **2025**, 44, 111889.
[27] Xu, H.; Zhu, J.; Zou, G.; Liu, W.; Li, X.; Li, C.; Ryu, G. H.; Xu, W.; Han, X.; Guo, Z. et al. Spatially bandgap-graded $mos_{2(1-x)}se_{2x}$ homojunctions for self-powered visible–near-infrared phototransistors. *Nano-Micro Letters* **2020**, 12, 26.
[28] Yagmurcukardes, M.; Qin, Y.; Ozen, S.; Sayyad, M.; Peeters, F. M.; Tongay, S.; Sahin, H. Quantum properties and applications of 2d janus crystals and their superlattices. *Applied Physics Reviews* **2020**, 7, 011311.
[29] Zhang, X.; Pang, R. T.; Hou, X. R.; Wang, S. D. Stacking-tailoring quasiparticle energies and interlayer excitons in bilayer janus mosse. *New Journal of Physics* **2021**, 23, 013003.
[30] Zhang, K.; Dandu, M.; Hung, N. T.; Zhang, T.; Barre, E.; Saito, R.; Kong, J.; Raja, A.; Huang, S. Optomechanical tuning of second harmonic generation anisotropy in janus mosse/$mos_2$ heterostructures. *ACS Nano* **2025**, 19, 38371-38380.
[31] Liu, M.; Wu, W.; Chen, Z.; Zhang, Y.; Yu, X.; Yang, S.; Wang, H.; Xu, F.; Chen, L.; Li, X. et al. Polarization-field-induced inequivalent exciton dynamics in janus moses/$mose_2$ heterostructures. *Nano Letters* **2025**, 25, 5723-5730.
[32] Lu, P.; Huangfu, Y.; Li, Z.; Zheng, X.; Huang, Z.; Zhang, Z.; Liu, S.; Zhang, Z.; Zhang, Z.; Li, J. et al. Bottom-up fabrication of bandgap-tunable patterned lateral $ws_2$-janus $w(s_{(x)}se_{(1-x)})se$ heterostructure arrays. *Small* **2026**, 22, e13894.
[33] Guo, Y. F.; Lin, Y. X.; Xie, K. C.; Yuan, B. A.; Zhu, J. D.; Shen, P. C.; Lu, A. Y.; Su, C.; Shi, E. Z.; Zhang, K. Y. et al. Designing artificial two-dimensional landscapes via atomic substitution. *Proceedings of the National Academy of Sciences of the United States of America* **2021**, 118, e2106124118.
[34] Yang, C.; Lin, Q.; Sato, Y.; Gao, Y.; Zheng, Y.; Wang, T.; Ma, Y.; Dai, W.; Li, W.; Maruyama, M. et al. Janus mosse nanotubes on 1d swcnt-bnnt van der waals heterostructure. *Small* **2025**, 21, e2412454.
[35] Miao, G.; Su, N.; Yu, Z.; Li, B.; Huang, X.; Zhong, W.; Guo, Q.; Liu, M.; Wang, W.; Guo, J. Doping elemental 2d semiconductor te through surface se substitutions. *Physical Review Letters* **2024**, 133, 236201.
[36] Li, K. H.; Xiao, F. P.; Guan, W.; Xiao, Y. L.; Xu, C.; Zhang, J. D.; Lin, C. F.; Li, D.; Tong, Q. J.; Li, S. Y. et al. Morphology deformation and giant electronic band modulation in long-wavelength $ws_2$ moiré superlattices. *Nano Letters* **2022**, 22, 5997-6003.
[37] Huang, X. Y.; Han, X.; Dai, Y. Y.; Xu, X. L.; Yan, J. H.; Huang, M. T.; Ding, P. F.; Zhang, D. C.; Chen, H.; Laxmi, V.; et al. Recent progress on fabrication and flat-band physics in 2D transition metal dichalcogenides moiré superlattices. *Journal of Semiconductors* **2023**, 44, 011901.
[38] Kresse, G.; Furthmuller, J. Efficient iterative schemes for ab initio total-energy calculations using a plane-wave basis set. *Physical Review B* **1996**, 54, 11169-11186.
[39] Kresse, G.; Joubert, D. From ultrasoft pseudopotentials to the projector augmented-wave method. *Physical Review B* **1999**, 59, 1758-1775.
[40] Perdew, J. P.; Burke, K.; Ernzerhof, M. Generalized gradient approximation made simple. *Physical Review Letters* **1996**, 77, 3865-3868.
[41] Grimme, S.; Antony, J.; Ehrlich, S.; Krieg, H. A consistent and accurate ab initio parametrization of density functional dispersion correction (dft-d) for the 94 elements h-pu. *Journal of Chemical Physics* **2010**, 132, 154104.
[42] Tersoff, J.; Hamann, D. R. Theory of the scanning tunneling microscope. *Physical Review B* **1985**, 31, 805-813.
[43] Heyd, J.; Scuseria, G. E.; Ernzerhof, M. Hybrid functionals based on a screened Coulomb potential. *The Journal of Chemical Physics* **2003**, 118, 8207-8215.

Just Accepted

# Electronic Supplementary Material

# Janus-engineering on the geometrical and electronic characteristics of the lateral and twisted $MoSeS/MoSe_2$ heterostructures investigated by scanning tunneling microscopy

Chenhao Zhang[1,§], Jiangpeng Zhou[1,§], Yanjun Li[1], Zongnan Zhang[1,2]✉, Mengyu Liu[1], Chunmiao Zhang[1], Xuanli Zheng[1], Feiya Xu[1], Lijing Kong[1], Xu Li[1], Zhiming Wu[1], Yaping Wu[1]✉ and Junyong Kang[1]

[1] *Department of Physics, Engineering Research Centre for Micro-Nano Optoelectronic Materials and Devices at Education Ministry, Fujian Provincial Key Laboratory of Semiconductor Materials and Applications, Xiamen University, Xiamen 361005, People's Republic of China*
[2] *Beijing National Laboratory for Condensed Matter Physics and Institute of Physics, Chinese Academy of Sciences, Beijing 100190, China*
[§] *These authors contributed equally to this work.*

✉Address correspondence to Yaping Wu, ypwu@xmu.edu.cn; Zongnan Zhang, zongnan@iphy.ac.cn

Supporting information to https://doi.org/10.26599/NR.2026.94909217

**Contents:**

Figure S1. Schematic diagram of improved mechanical exfoliation for STM characterization.
Figure S2. X-ray photoelectron spectroscopy (XPS) characterization.
Figure S3. Effect of lattice mismatch in $MoSeS/MoSe_2$ heterostructure.
Figure S4. Planar-averaged electrostatic potential.
Figure S5. Band structures of the $MoSeS/MoSe_2$ heterostructures.

Just Accepted



Address correspondence to First A. Firstauthor, email1; Third C. Thirdauthor, email2

1. Improved mechanical exfoliation for sample preparation

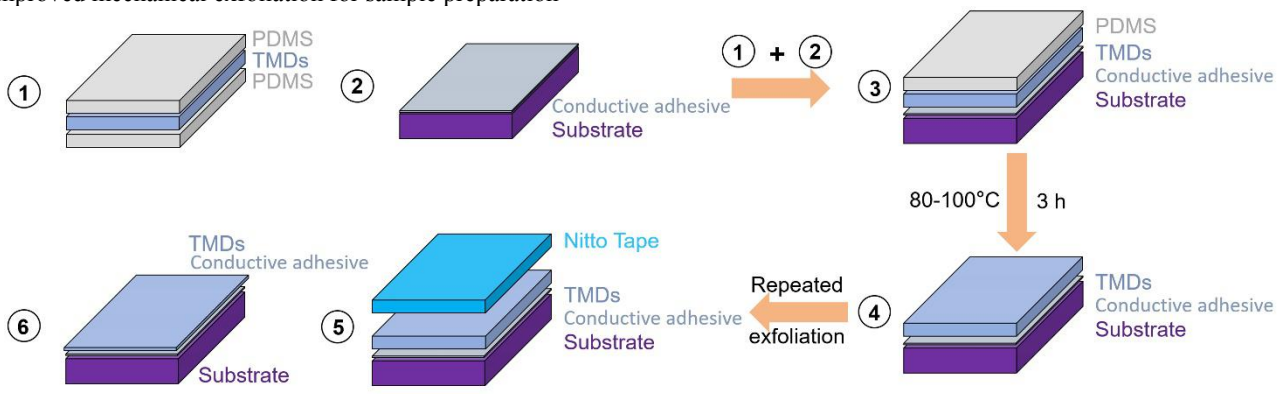



**Fig. S1.** Schematic diagram of improved mechanical exfoliation for STM characterization.

A bulk $MoSe_2$ crystal was first sandwiched between two polydimethylsiloxane (PDMS) films for flattening and securing the crystal. It was then transferred onto a substrate pre-coated with conductive adhesive, followed by thermal curing to enhance the interfacial adhesion. After removal of the PDMS film, repeated exfoliation was performed using Nitto tape until atomically thin flakes were obtained on the conductive substrate, as identified under an optical microscope by their light-blue or nearly transparent contrast in Fig. 1(a).

2. X-ray photoelectron spectroscopy (XPS) characterization

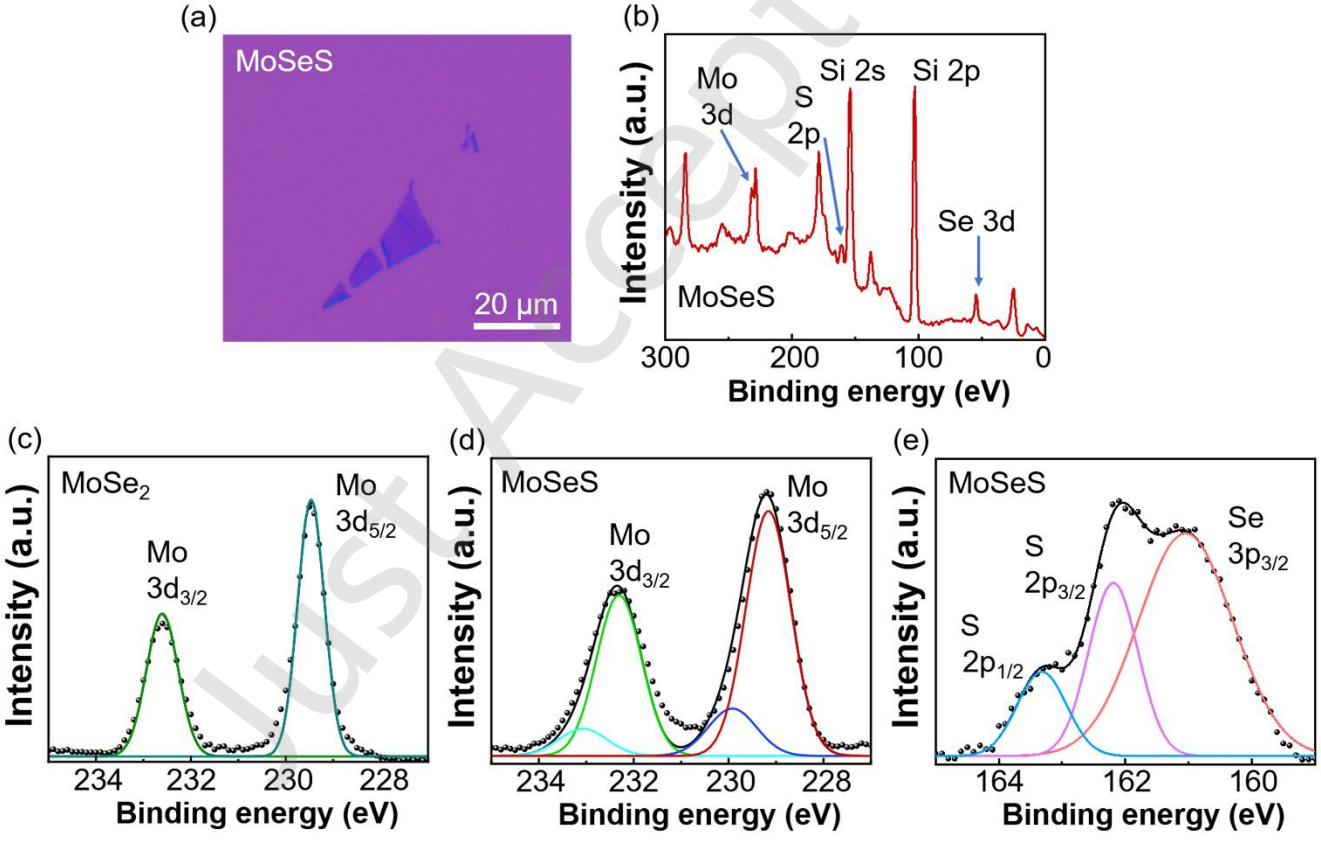



**Fig. S2.** XPS characterization of MoSeS and $MoSe_2$ monolayer. (a) Optical image of MoSeS monolayer on a $SiO_2$/Si substrate. (b) XPS survey spectrum of the monolayer MoSeS. (c) High-resolution Mo 3d spectrum of $MoSe_2$. (d) High-resolution Mo 3d spectrum of MoSeS. (e) High-resolution S 2p spectrum of MoSeS. The black dots and colored solid lines represent the experimental data and the corresponding fitted curves, respectively.

For quantification of the sulfur- substitution ratio, exfoliated monolayer $MoSe_2$ was transferred onto a $SiO_2$/Si substrate (Fig. S2(a)) and subsequently converted into MoSeS controllably via the hydrogen-plasma-assisted sulfurization strategy. The XPS survey spectrum confirms the presence of Mo, S, and Se elements (Fig. S2(b)), with the characteristic Mo 3d, S 2p, and Se 3d peaks located at approximately 230 eV, 162 eV, and 55 eV, respectively. As a reference, the high-resolution Mo 3d spectrum of $MoSe_2$ exhibits a well-defined spin-orbit doublet, with the Mo $3d_{5/2}$ and Mo $3d_{3/2}$ peaks centered at 229.46 eV and 232.60 eV, respectively, and the corresponding full widths at half maximum (FWHMs) of 0.66 eV and 0.79 eV (Fig. S2(c)). In comparison, deconvolution of the asymmetric Mo 3d core- level spectrum for the MoSeS monolayer yields two sets of peaks associated with Se- Mo- Se and Se- Mo- S bonding configurations (Fig. S2(d)). The peaks at 229.16 eV and 232.31 eV (FWHM = 1.12 eV) are assigned to



Just Accepted

$MoSe_2$- like species, whereas those at 229.92 eV and 233.07 eV (FWHM = 1.20 eV) stem from sulfur- substituted Se- Mo- S bonding environments. Compared with the reference $MoSe_2$, the increased peak widths in MoSeS indicate a broadened distribution of the local chemical environment of Mo associated with S substitution. Quantitative analysis based on the peak areas yields a $MoSe_2$-to-MoSeS ratio of approximately 7:1, indicating a sulfur substitution level of ~15%. Furthermore, the high-resolution S 2p spectrum further exhibits characteristic S 2p spin-orbit doublet, with the S $2p_{3/2}$ and S $2p_{1/2}$ peaks located at 162.19 eV and 163.32 eV, respectively (Fig. S2(e)), further confirming the incorporation of S into the $MoSe_2$ lattice.

3. Effect of lattice mismatch in MoSeS/$MoSe_2$ heterostructure

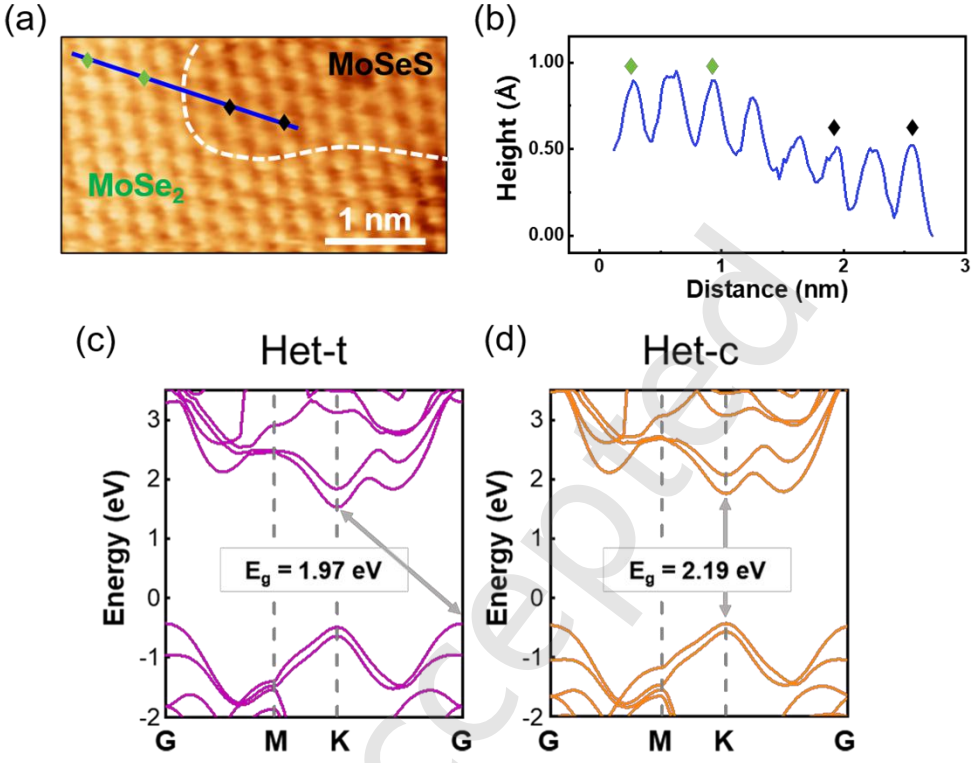



**Fig. S3.** Effect of lattice mismatch on the band structures of MoSeS/$MoSe_2$ heterostructure. (a) STM image of the MoSeS/$MoSe_2$ lateral heterostructure. (b) Height profile along the blue line in (a). (c, d) The band structures of MoSeS/$MoSe_2$ heterostructure with tensile and compressive lattice constants of 3.30 Å and 3.23 Å, respectively.

S substitution triggers the formation of Janus MoSeS, which simultaneously introduces intrinsic lattice strain in the heterostructure. As displayed in Figs. S3(a) and (b), the $MoSe_2$ and MoSeS regions possess distinct lattice constants of 3.27 Å and 3.20 Å, respectively, giving rise to a lattice mismatch of 2.1%. To clarify the lattice-induced modulation of electronic properties, the band structures of MoSeS/$MoSe_2$ heterostructures under various lattice strains were systematically calculated. When the lattice constant is expanded to that of $MoSe_2$ (Fig. S3(c)), the MoSeS/$MoSe_2$ heterostructure (denoted as Het- t) retains its indirect bandgap with the CBM and VBM locating at the K and Γ points, respectively, while the bandgap decreases to 1.97 eV. Upon compressing the lattice constant to that of MoSeS, the MoSeS/$MoSe_2$ heterostructure (denoted as Het- c) becomes a direct- bandgap semiconductor with a bandgap of 2.19 eV, in which both the CBM and VBM are positioned at the K point (Fig. S3(d)). Overall, though the lattice strain influences the VBM location of the MoSeS/$MoSe_2$ heterostructure, it induces only a moderate variation in its bandgap amplitude.

Just Accepted

4. Planar-averaged electrostatic potential

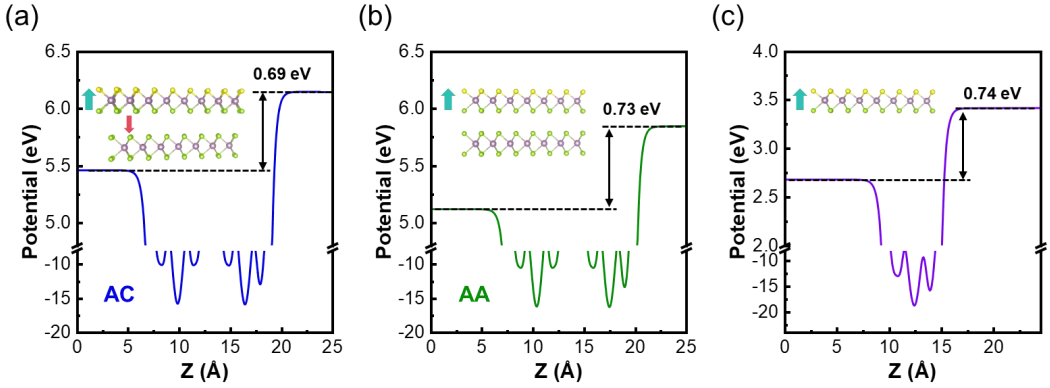



**Fig. S4.** Planar-averaged electrostatic potentials along the out-of-plane (Z) direction of (a) the AC- and (b) AA-stacked MoSeS/$MoSe_2$ heterostructures and (c) MoSeS monolayer, the green and red arrows mark the direction of intrinsic built-in electric field of MoSeS and the interlayer polarized field.

5. Band structures of the MoSeS/$MoSe_2$ heterostructures

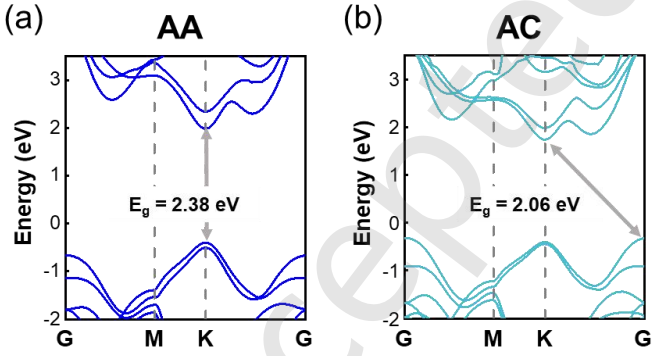



**Fig. S5**. Calculated band structures of the MoSeS/$MoSe_2$ heterostructures with (a) AA and (b) AC stackings.

Just Accepted